

**\*Abstract**

[Click here to download Abstract: Abstract.pdf](#)

**Abstract:** Subduction zones are the primary means of recycling crustal material into the mantle, yet observations at many subduction zones suggest not all subducted material reaches mantle depths. Discrete element numerical models are used to understand how tectonic underplating, the subcretion of subducted sediments from the top of the downgoing plate to the bottom of the overriding plate, drives upper plate faulting and uplift patterns. Our models attempt to mimic the processes occurring at Raukumara Peninsula, New Zealand, a location of proposed underplating. We also apply differential surface erosion, landsliding, and several variations of upper plate faulting, motivated by processes occurring on Raukumara Peninsula, to test how these factors may affect the underplating system. We find that in an underplating-only system antiformal uplift occurs above the underplated body with trenchward displacement dominating outboard of the uplifting region. These two zones are separated by a normal fault, the location of which determines the relative amounts of uplift and horizontal trenchward displacement. Most of the tested factors in this system (landsliding, upper plate faulting, subduction-interface induced faulting) have a minimal effect on the overall system evolution, but differential surface erosion shifts the zone of most rapid uplift towards the area that experiences the greatest amount of erosion. This work suggests that in the absence of a strong differential erosion forcing, antiformal uplift should be expected on Raukumara Peninsula, but if differential erosion is present, then asymmetrical uplift would be predicted. Both shapes of uplift have previously been proposed by previous investigators based on different field measurements.

1    **Controls on Uplift Patterns on the Raukumara Peninsula, New**  
2    **Zealand: Insights from Discrete Element Modeling**

3    William Farrell<sup>a</sup>, Julia Morgan<sup>a\*</sup>, Harsha Vora<sup>a</sup>

4    <sup>a</sup>Rice University, Department of Earth, Environmental, and Planetary Sciences, Houston, Texas,  
5    USA

6    \*Corresponding author at: EEPS Dept, MS-126, Rice University, 6100 Main St, Houston, TX,  
7    77005

8    Email address: morganj@rice.edu

9    **Keywords:** Raukumara Peninsula, Discrete Element Method, underplating, uplift, erosion,

10    **Highlights:**

- 11    • Discrete Element Method (DEM) modeling is used to replicate underplating, the  
12    subcretion of sediments to the bottom of an overriding plate.
- 13    • Antiformal uplift is seen above the zone of active underplating in our model
- 14    • Surface erosion, when preferentially applied to one side of the underplating zone, creates  
15    asymmetrical uplift.
- 16    • Uplift is most rapid beneath the most rapidly eroding zone
- 17    • Surficial landsliding and upper plate faulting do not appear to exhibit control on  
18    underplating-driven uplift patterns.

19    **Abstract:** Subduction zones are the primary means of recycling crustal material into the mantle,  
20    yet observations at many subduction zones suggest not all subducted material reaches mantle  
21    depths. Discrete element numerical models are used to understand how tectonic underplating, the  
22    subcretion of subducted sediments from the top of the downgoing plate to the bottom of the  
23    overriding plate, drives upper plate faulting and uplift patterns. Our models attempt to mimic the  
24    processes occurring at Raukumara Peninsula, New Zealand, a location of proposed underplating.  
25    We also apply differential surface erosion, landsliding, and several variations of upper plate  
26    faulting, motivated by processes occurring on Raukumara Peninsula, to test how these factors  
27    may affect the underplating system. We find that in an underplating-only system antiformal

28 uplift occurs above the underplated body with trenchward displacement dominating outboard of  
29 the uplifting region. These two zones are separated by a normal fault, the location of which  
30 determines the relative amounts of uplift and horizontal trenchward displacement. Most of the  
31 tested factors in this system (landsliding, upper plate faulting, subduction-interface induced  
32 faulting) have a minimal effect on the overall system evolution, but differential surface erosion  
33 shifts the zone of most rapid uplift towards the area that experiences the greatest amount of  
34 erosion. This work suggests that in the absence of a strong differential erosion forcing,  
35 antiformal uplift should be expected on Raukumara Peninsula, but if differential erosion is  
36 present, then asymmetrical uplift would be predicted. Both shapes of uplift have previously been  
37 proposed by previous investigators based on different field measurements.

### 38     **1. Introduction**

39     Tectonic underplating, the transfer of material at depth from the top of a subducting slab to  
40 the bottom of the overriding plate, has been postulated to occur at multiple subduction zones  
41 around the world (e.g. Adam and Reuther, 2000; Calvert et al., 2011; Clift and Hartley, 2007;  
42 Fuis et al., 2008; Henrys et al., 2013; Kimura et al., 2006; Krawczyk et al., Moore et al., 1991;  
43 Kimura et al., 2010; Krawczyk et al., 2006; Moore et al., 1991; Platt, 1986; Sutherland et al.,  
44 2009). Geophysical images from these locales suggests that sediments are transported from the  
45 seafloor to deeper depths beneath the overriding plate within a sediment channel. This process is  
46 favored along erosive subduction margins. To accommodate underplating at depth, the  
47 decollement is thought to step downward from the top of the sediment channel to the top of the  
48 downgoing plate for reasons that are poorly understood. This allows an imbricated package of  
49 sediment to be subcreted to the bottom of the overriding plate. Commonly these underplated  
50 sediments are located below actively rising surface topography responding to the influx of  
51 crustal material from below.

52     Geophysical observations supporting active underplating at depth have been made over the  
53 Raukumara Peninsula on the North Island of New Zealand. The North Island of New Zealand  
54 (Figure 1a) sits along the Hikurangi margin, a continent-ocean convergence zone where the  
55 Pacific Plate has been subducting beneath Australian Plate continental crust for at least the past  
56 20 my (Ballance, 1976; Kamp, 1999; Rait et al., 1991). The margin is characterized by the  
57 subduction of a region of overthickened Pacific Plate crust known as the Hikurangi Plateau. The

58 main onshore geologic features of the North Island are the Axial Ranges and the Taupo Volcanic  
59 Zone (Figure 1b). The North Island's Axial Ranges run north to south along the center of the  
60 island. Composed of relatively resistant Cretaceous greywacke, they form the “backbone” and  
61 topographic high of the island (Litchfield et al., 2007). The Taupo Volcanic Zone and coincident  
62 Taupo Rift lie to the west of the Axial Ranges and represent an onshore-offshore back-arc  
63 spreading center currently extending at ~15 mm/yr (Nicol et al., 2007) (Figure 1b). The  
64 Raukumara Peninsula, composed of the Axial Ranges and exposed forearc of the Northern  
65 Hikurangi margin, sits in the northeast corner of the North Island. The main topographic feature  
66 on the peninsula is the Raukumara Range, actively deforming mountains with a maximum height  
67 of 1755 m that are composed primarily of Cretaceous-age Torlesse Greywacke (Wilson, 2006).  
68 To the east of the Raukumara Range there are two main packages of sedimentary rocks, the East  
69 Coast Allochthon and a unit of Neogene Sediments (Thornley, 1996) (Figure 2a). The East Coast  
70 Allochthon is an early Miocene thrust sheet composed of marine sediments, which was probably  
71 emplaced at the initiation of subduction and has a very narrow surface exposure between the  
72 greywacke and Neogene sediments (Scherwath et al., 2010). Occupying the eastern half of the  
73 peninsula are Neogene marine sediments, which overlie the Allochthon to the east and are  
74 faulted against it to the west (Reyners et al., 1999) (Figure 2a).

75 Beneath the peninsula, subducted sediments along the northern Hikurangi margin are  
76 interpreted to be underplated at a depth that coincides with the Moho of the overriding Australian  
77 plate (Sutherland et al., 2009). The overlying Raukumara Mountains exhibit anomalously rapid  
78 uplift relative to adjacent regions, leading researchers to invoke underplating as a possible driver  
79 for uplift of the range (Bassett et al., 2010; Eberhardt-Phillips and Chadwick, 2002; Heise et al.,  
80 2012; Walcott, 1987). The shape of this uplift since the Pleistocene is debated, as workers have  
81 put forward competing models: uplift patterns may be antiformal (Litchfield et al., 2006) or  
82 asymmetrical (Wilson, 2006) (Figure 3), reflecting other processes that accompany subduction.  
83 For example, gravitationally driven extension along the trenchward side of Raukumara Range,  
84 documented geodetically (Thornley, 1996), may be influencing strain localization above the  
85 underplated material. This extension is thought to be accommodated along the Whakoau fault, a  
86 listric trenchward-dipping normal fault daylighting at the Torlesse Greywacke/Neogene  
87 Sediments contact (Thornley, 1996).

88 One of the primary factors thought to modulate tectonic uplift is surface erosion (e.g. Avouac  
89 and Burrov, 1996; Beaumont et al., 1992; Koons, 1990; Thiede et al., 2004; Whipple, 2009).  
90 Workers have concluded that erosion locally enhances uplift in the most rapidly eroding areas by  
91 reducing overburden, thereby modifying the uplift patterns compared with the uneroded system.  
92 Preferential erosion of weaker Neogene sediments relative to Torlesse Greywacke (Figure 2a)  
93 has been proposed as a control on the shape of uplift on Raukumara Peninsula (Wilson, 2006).  
94 Similar uplift patterns have been seen in areas undergoing shallow landsliding (e.g. Burbank et  
95 al., 1996; Kobor and Roering, 2004), which also works as a surficial mass transfer process  
96 similar to erosion and is also capable of locally enhancing uplift. None of this work on tectonic-  
97 surface process interactions has focused on areas of underplating-driven uplift and it is therefore  
98 an open question to what extent these processes are controlling uplift on Raukumara Peninsula.

99 Numerical modeling can help fill this void in our understanding of the effects of tectonic  
100 underplating on the structural evolution of the overriding plate. It allows us to test various  
101 hypotheses that have been put forward to explain the patterns of uplift across the Raukumara  
102 Range, and the structural controls on those patterns. In this study, we first establish a reference  
103 for a system subjected to underplating only, and then examine the effects of various additional  
104 factors on that system, to determine if they might explain the controls on asymmetric vs  
105 antiformal uplift. We find that in an underplating-only model we can expect antiformal uplift  
106 centered directly above the underplating body, whereas differential surface erosion of the  
107 uplifting region can enhance uplift preferentially beneath the eroding region, leading to an  
108 asymmetrical uplift pattern. Other factors, such as surficial landsliding and upper plate faulting,  
109 appear to have less control on uplift patterns in our underplating system.

110 We employ RICEBAL, a Discrete Element Method (DEM) modeling program developed at  
111 Rice University, to explore these phenomena. DEM has been employed previously to study  
112 large-scale structural evolution (Dean et al., 2013; Katz et al., 2014; Morgan, 2015; Morgan and  
113 McGovern, 2005; Naylor et al., 2005) but its application to underplating-driven uplift is novel.  
114 Using these tools, our study seeks to enhance our understanding of underplating-driven uplift and  
115 the effects surficial processes and upper plate strength heterogeneities have on the underplating  
116 process and resulting uplift patterns. We base our model on the Raukumara Peninsula, North  
117 Island, New Zealand, where strong arguments are made that surface processes play a major role

118 (Wilson, 2006) in shaping uplift. We then compare our results to other regions where active  
119 underplating has been interpreted.

120 **2. Methods**

121 **2.1 Discrete Element Method (DEM)**

122 The Discrete Element Method (DEM) (e.g. Cundall and Strack, 1979), a particle-based  
123 numerical modeling technique employed in this study, uses assemblages of particles to simulate  
124 deformation in granular materials. A 2-D “numerical sandbox” is built to desired scale and  
125 particles are generated and allowed to settle under gravity. At each discrete time step in the  
126 model, the forces acting on each particle due to gravity, boundary conditions, and other particles,  
127 are calculated. Contact forces arise from particle-particle interactions and are calculated using  
128 Hertz-Mindlin contact theory (Guo and Morgan, 2007; Morgan, 1999, 2015). Body forces act on  
129 the particle centroids due to gravity. The summed forces acting on each particle allow  
130 displacements to be calculated using Newton’s equations of motion (Guo and Morgan, 2007;  
131 Morgan, 1999, 2015). In this way, particle assemblages can evolve and deform. Interparticle  
132 bonding imparts cohesion to the assemblage, and bond breakage under tension or shear allows  
133 localized faults to develop. Thus, assemblage strength depends primarily on interparticle friction  
134 ( $\mu$ ) and interparticle bond strengths. Further details of the modeling approach are described  
135 elsewhere (Morgan, 1999, 2015). The DEM code employed for this study, RICEBAL (Morgan,  
136 2015), is based upon an older version of TRUBAL (Cundall and Strack, 1979).

137 **2.2 Experimental Setup**

138 Our reference 2-D model configuration is shown in Figure 4 and defines the basis for all  
139 models presented here. The initial domain is 170 km x 50 km, and is a simplified representation  
140 of the most seaward portion of the Pacific-Australian plate boundary (Figure 4). A horizontal  
141 fixed wall serves as the top of the incoming Pacific Plate. The overriding Australian Plate is  
142 constrained by a fixed vertical wall at the right edge of the model and represented by a wedge  
143 that tapers to the left. To build this wedge, particles are deposited above the horizontal boundary,  
144 and allowed to settle under gravity. This domain is then sculpted into a wedge designed to  
145 approximate the surface geometry of a cross-section across the northern Hikurangi margin. The  
146 model is composed of two domains of particles with contrasting properties (Table 1). The top

147

148

149

150 **Table 1:** Properties of Model Materials

Particle Type	Particle density (kg/m <sup>3</sup> )	Particle Radius (m)	Particle shear modulus (MPa)	Poisson's Ratio	Bond Young's Modulus (MPa)	Bond Shear Modulus (MPa)	Bond Tensile Strength (MPa)	Bond Cohesion (MPa)	Interparticle Friction Coefficient
Upper layer of wedge	2500	80 - 100	2900	0.2	10000	300	300	800	0.3
Lower layer of wedge	2500	80 -100	2900	0.2	N/A	N/A	N/A	N/A	0.2 (Except at base of toe where 0.6)
Underplated material	2500	80 - 100	2900	0.2	N/A	N/A	N/A	N/A	0.0

151 \*Where no bonds are present bond parameters are listed as "N/A"

152

153

154

155

156

157

158

159

160

161

162

163

164

165

166

167 domain in the wedge is bonded using interparticle bond parameters constrained by the  
168 calibrations described below, and thus behaves in a brittle manner; interparticle friction is set to  
169 0.3. The bottom domain is unbonded to enable more distributed deformation, to approximate  
170 lower crustal ductile flow; the interparticle friction coefficient of the lower domain is set to 0.2.  
171 Basal friction of the wedge is 0.3, except for the leftmost 30 km, where a basal friction of 0.6 is  
172 applied to prevent wedge collapse. It is worth noting that our wedge sits on a flat base for  
173 modeling simplicity, rather than the curved downgoing plate which exists in nature. We expect  
174 that this will enable more trenchward displacement of wedge material than would otherwise  
175 happen in nature. For example, the relief between our model trench and the top of our model is  
176 15 km, while in nature there is scarcely 5 km of relief between the Hikurangi margin trench and  
177 the highest point of the Raukumara Range. This is due to our use of a wedge with a flat base in  
178 the model while in nature this base is curved. We discuss the implications of this simplification  
179 later.

180 A third domain of particles is created below the horizontal base, a proxy for the underplated  
181 material that intrudes into the overlying wedge. The domain size is 10 km thick by 40 km wide,  
182 corresponding to the approximate size of the underplated sediment body beneath Raukumara  
183 Peninsula (Eberhardt-Phillips and Chadwick, 2002; Heise et al., 2012). These underplating  
184 particles are left unbonded and frictionless.

185 Each model run initiates by applying a vertical velocity to the underplating body so it will  
186 intrude through the base of the wedge. The vertical velocity is set to 50 m/image, and for every  
187 50 m of rise of the underplated body, particle data are recorded for future calculations of stress,  
188 strain, and particle position. As particles enter the wedge domain through the base, they are  
189 “released” from the imposed velocity so that they can move within the wedge in response to the  
190 local stress field. The underlying particles continue to rise upward, pushing the newly released  
191 particles into the wedge. This maintains a constant influx of underplated material, independent of  
192 the various forcings applied to the system.

193 We first conduct an underplating-only reference simulation, and then systematically add  
194 erosion, landsliding, and material properties heterogeneities that may exist or act upon the  
195 Raukumara Peninsula system. We document how these surface and upper plate processes affect  
196 the surficial uplift and structural evolution of our underplating system.

197    **2.3 Material Strength Calibrations**

198    As seen in Figure 2a and b, Torlesse Greywacke is the dominant rock composing the  
199    Raukumara Range and underlying the on- and offshore accretionary prism. Because the Torlesse  
200    unit is thought to be the dominant lithology in this system, its strength and properties will define  
201    the behavior of the overall system. Thus, we seek to define mechanical properties of the bonded  
202    upper half of our numerical wedge material to best replicate those documented for this unit. A  
203    compilation of results of previous uniaxial and biaxial compression tests on samples of Torlesse  
204    Greywacke provide representative unconfined compressive strengths (UCS) and Coulomb failure  
205    envelopes for this material (Table 2) (Stewart, 2007; Mielke et al., 2016; McNamara et al., 2016).  
206    We conducted a suite of numerical uniaxial consolidation and confined biaxial consolidation  
207    experiments, using a range of interparticle friction and bond parameters to find a match the  
208    experimental properties. We obtained a set of parameters that resulted in a UCS and Coulomb  
209    failure envelope similar to those published for Torlesse Greywacke. Further details about our  
210    calibration study can be found in Farrell (2018).

211    These derived parameters were used as a starting point for the wedge material strengths,  
212    although we recognize that the mass rock properties of these materials may be lower than those  
213    of discrete experimental samples. A first order assessment of the appropriateness of the chosen  
214    parameters is the nature and distribution of deformation in the shallow upper plate, e.g., a  
215    distribution of extensional fractures and faults across the uplifted region as observed in nature.  
216    The original bond properties resulted in isolated tears that spanned the entire domain, suggesting  
217    that the bulk cohesion was too high. Thus, we decreased the Torlesse Greywacke bond tensile  
218    strengths incrementally, until the simulations yielded more realistic fractures and faults near the  
219    surface of the wedge above the underplating body. This reduction in strength is justified on the  
220    presence of heterogeneities, fractures, and faults in rock masses over large spatial scales, which  
221    make them weaker than a small sample of the same rock would suggest (e.g. Barton and Brandis,  
222    1982). Table 1 shows the final particle and bond values used here.

223    The properties of the unbonded lower half of the wedge, a proxy for the ductile lower  
224    crust, are less well constrained, and so were not calibrated explicitly. Instead, we tested several  
225    different interparticle friction values, starting with a frictionless system. Interparticle friction was  
226    increased in increments of 0.1 until a lower limit was found which provided enough strength to

227

228 **Table 2:** Material Strength Calibration Results

<b>Study</b>	<b>Cohesion (MPa)</b>	<b>Angle of Internal Friction</b>
(Stewart, 2007)	48.2	34.6
(Stewart, 2007)	48.0	45.0
(McNamara et al., 2014)	49	44
<b>Model Material</b>	<b>50</b>	<b>38</b>

229

230

231

232

233

234

235

236

237

238

239

240

241

242

243

244

245

246 avoid massive slumping and failure. This lower limit was reached at an interparticle friction of  
247 0.2 (Table 1).

248 **2.4 Experimental Results**

249 We carried out five simulations to understand the behavior of the reference system, and  
250 to explore the effects of several internal and surficial processes. The variations to the system  
251 were introduced by capturing particles within defined regions, and either removing them (e.g.,  
252 erosion) (Figure 5a), changing their properties (e.g., interparticle friction values, bond properties,  
253 etc.) (Figure 5b), or displacing the boundary materials (Figure 56).

254 Erosion was introduced by defining a four-sided polygon near the surface of the wedge  
255 and removing all particles that enter the polygon at set intervals throughout the model run.  
256 Particles were removed at eight equally-spaced intervals in the erosion model described below.

257 Landsliding was imposed by a listric fault that daylighted at the approximate location of  
258 the Whakoau fault, introduced halfway through the model run. This fault is approximately 3  
259 particle diameters thick. All bonds were broken within the fault zone and interparticle friction  
260 was reduced to zero. This favors slip both between particles in the fault zone and at the top and  
261 base of the unbonded fault zone.

262 Faults of different orientations were imposed in a similar way to landsliding, with bonds  
263 being broken and interparticle friction reduced to zero within predefined four-sided polygons  
264 selected to simulate specific fault geometries.

265 Finally, we tested the effects of pre-existing deformation, induced here by displacing a  
266 subducting plate along the basal interface. A 2 km thick, 50 km long block of material was  
267 displaced along the length of the base of the wedge. This displacement occurred before  
268 underplating began in an attempt to create realistic structures and upper plate damage that might  
269 have developed during subduction.

270 **2.5 Tracking Strain and Uplift**

271 The spatial distribution of strain in two dimensions is analyzed throughout the model.  
272 Plots of distortional strain over the model domain are derived from the local strain tensor based  
273 on particle displacements (Morgan, 2015). Distortional strain is represented here as the second

274 invariant of the deviatoric strain tensor. Generic Mapping Tools (Wessel and Smith, 1995) are  
275 employed to plot the strain fields.

276 Uplift plots are created by tracking the positions of individual particles every 10 images  
277 in the model (equivalent to 0.5 km of vertical displacement on the underplating body) using  
278 Matlab. These plots track particles that started at approximately 10 km, 5 km, and 2 km depths,  
279 and at x-positions initially spaced from 15 to 25 km apart between 50 and 150 km from the left  
280 side of the model. Particle x and y positions through time are then overlain on plots of the final  
281 distortional strain to demonstrate their correspondence to upper plate deformation; open  
282 diamonds denote the initial particle positions, and closed diamonds show the final particle  
283 positions.

284 **3. Results**

285 **3.1 Underplating-Only (Reference) Model**

286 In our reference model, deformation is driven solely by emplacing the underplated body  
287 into the two-layer upper plate from below. Underplating in the reference model results in a  
288 roughly antiformal topographic shape with a pronounced central peak (Figure 7a). Away from  
289 the central peak, topography is higher on the model's inboard side. Surface topography is not  
290 mirrored by the boundary with the ductile layer below, which shows a much smoother antiform  
291 and lacks a central peak. The underplated body remains roughly rectangular, but shows some  
292 trenchward displacement of material at the outboard end. The distortional strain plot for this  
293 reference model (Figure 7b) shows a few high angle normal faults that dip trenchward, just  
294 outboard of the underplated zone. A single high angle reverse fault bounds the inboard edge of  
295 the underplated zone, and a shallow graben structure occurs within the uplifted zone.

296 The uplift data (Figure 7b) show that all crustal levels monitored exhibit similar  
297 displacement patterns for a given horizontal position in the model. Outside of the deformation  
298 zone, trenchward of the normal faults, material was displaced uniformly trenchward via slip on  
299 these normal faults. Directly above or on the inboard edge of the underplated body, particle  
300 trajectories are vertical, and inboard of the reverse fault to the right, particles did not move. One  
301 observed difference in particle trajectories occurs at  $x = 115$  km. The particle from mid-crustal  
302 levels (10km depth) shows a vertical trajectory, whereas particles at the shallower (5 km depth)

303 and shallowest (2 km depth) crustal levels initially rise, but then proceed to move trenchward in  
304 paths similar to the more outboard material. The particles move trenchward once captured by the  
305 high angle normal faults outboard of the uplifting zone.

306 **3.2 Landsliding Model**

307 The introduction of a frictionless listric interface halfway through the model run (shown  
308 in green, Figure 7c) defines a surficial landslide detachment with a geometry similar to the  
309 Whakoau Fault. The overlying material is able to slide trenchward along this zone of weakness  
310 once sufficient topography is built to drive gravitational displacement. Compared to the  
311 reference model, surface topography increases more gradually, ramping up to the central high  
312 point above the underplating zone (Figure 7c), in contrast to the more antiformal topography  
313 seen in the reference model. Displacement and trenchward slumping occur along the imposed  
314 landslide surface. The distortional strain plot for this model (Figure 7d) looks similar to the  
315 reference model with a few key differences. First, the thick normal faults bounding the left side  
316 of the deformation zone now encroach further inboard and at a lower angle, using the predefined  
317 landsliding surface to their kinematic advantage. Second, the high angle reverse fault on the right  
318 edge of the deformation zone now has a normal fault splaying off it and verging back into the  
319 center of deformation. The underplated body in this landsliding model has deformed similarly to  
320 the reference models.

321 Uplift within the landsliding model (Figure 7d) looks similar to the reference model with  
322 a few important differences. At the shallowest-crustal levels (black uplift paths in Figure 6d), the  
323  $x=125$  km particle, which has a near vertical trajectory and the maximum amount of uplift in the  
324 reference model, experiences trenchward displacement along with all the particles to its left. This  
325 is due to its incorporation into the landslide. The tracked particle further inboard at  $x=135$  km  
326 experiences more uplift by comparison to the reference model. A similar phenomenon is evident  
327 at the mid-crustal level (green uplift paths in Figure 7d), where the  $x=125$  km particle translates  
328 trenchward in the landsliding model but not in the reference model.

329 **3.3 Differential Erosion Model**

330 Differential erosion is imposed by defining “Erosion” and “No Erosion” zones (Figure  
331 7e). The erosion zone roughly spans the eastern half of the onshore portion of Raukumara

332 Peninsula, consistent with the zone of more erodible sediment east of the highest topography  
333 (Wilson, 2006). All material that moves above the prescribed surface underneath the “Erosion  
334 Zone” in Figure 7e is removed at eight equally spaced intervals during the model run. In  
335 response to the imposed erosion, the highest topography occurs farther inboard than for the  
336 previous two models, outside of the erosion zone. This contrasts with the reference model, where  
337 the highest topography lies within what would be the inboard edge of the erosion zone.  
338 Compared to the reference model, fewer discrete faults form overall (Figure 7f). On the  
339 trenchward side of the underplating zone, the main normal fault forms at a higher angle and does  
340 not penetrate as far inboard as compared to the reference model. The main fault on the right side  
341 of the uplift, however, now has normal rather than thrust displacement and occurs at a lower  
342 angle compared to its reference model counterpart.

343 Uplift data for the erosion model shows stark differences from the reference and landslide  
344 model. Specifically, the  $x=115$  km mid-crustal (green) particle (Figure 7f) shows the greatest  
345 uplift distance of any particle monitored in the study. This implies that the spatial distribution of  
346 uplift rates has shifted. In all other models outlined here the  $x=125$  km particle, located directly  
347 above the underplated body, shows the most uplift. But in the erosion model the differential  
348 erosion and reduction in overburden drives more rapid uplift in the trenchward region, and uplift  
349 on the inboard side of the underplating is reduced. The same is true for the shallow crustal  
350 particle at  $x=125$  km (Figure 7f). Note that many particles, especially at the shallowest crustal  
351 level (Figure 7f) were eroded and removed from the system, and thus show seemingly minimal  
352 displacements.

### 353 **3.4 Pre-Existing Faults Model**

354 To test if the presence of predefined planes of weakness will affect the evolution of the  
355 system, discrete faults are introduced into the model. The faults are defined by prescribing linear  
356 zones of weakness in the general vicinity of large mapped faults on the Raukumara Peninsula  
357 (Mazengarb and Spaden, 2000; Nicol and Beaven, 2003; Wilson, 2006; Barnes et al., 2010).  
358 These faults dip trenchward in the frontal portion of the wedge and are oriented nearly vertical  
359 adjacent to the back arc (Figure 2b). The faults are represented as 1 km thick unbonded  
360 rectangular regions, with interparticle friction set to zero. The back-arc faults are 10 km long,  
361 and the reverse faults in the frontal part of the wedge are slightly less than 5 km long.

362        The final model configuration and distortional strain plots (Figure 7g and h) show that  
363    only the most trenchward reverse fault and the high angle fault closest to the underplating body  
364    experienced any appreciable motion on them. The reverse fault acted as a second décollement for  
365    material slumping trenchward while the high angle fault allowed for slightly more uplift on the  
366    backside of the uplifting zone. When compared to the reference model, the normal faults  
367    bounding the left-edge of the uplifting zone appear more well-spaced and discrete while the high  
368    angle fault bounding the right-side of the uplifting zone chooses to take advantage of the  
369    imposed fault. Surficial uplift occurs in a wide zone, but with lower relief than in the reference  
370    model. The rest of the imposed faults remain virtually dormant for the duration of the model run.

371        The uplift data for this model (Figure 7h) also looks very similar to the reference model  
372    results: antiformal mid-crustal uplift, trenchward horizontal displacement from material on the  
373    slope, and a lack of movement inboard of the uplifted zone. In addition, the shallower material  
374    mimics that of the reference model. As particles on the outboard side of the uplifted zone move  
375    towards the surface they are more likely to displace trenchward along with the ramp material. In  
376    short, uplift paths between the imposed faulting model and the reference model do not appear to  
377    differ in a significant way.

378    **3.5 Subduction Interface Model**

379        The subduction interface model is distinct from the other models in that the starting  
380    configuration just before underplating (Figure 6f) is highly deformed and, as a result, the initial  
381    shape of the wedge is very different. This deformation is the result of the displacement of a block  
382    of material along the base of the wedge, moving from left to right (Figure 6). The goal is to  
383    recreate the deformation that would occur during subduction below the wedge prior to  
384    underplating, to determine if it influences underplating and uplift patterns. The leftmost portion  
385    of the wedge, where the ramp was initially, is now marked by a combination of high angle faults  
386    and conjugate fractures. Predictably, the pre-underplating deformation is more intense near the  
387    base of the wedge. Moving inboard, the high angle fractures in the unbonded material remain  
388    consistent throughout the wedge but the upper bonded portion shows minimal damage in the  
389    thickest portion of the upper plate (Figure 6f).

390        Underplating into the already highly deformed model causes a surficial expression with a  
391    pronounced ramp evident in both the upper and lower layers (Figure 7i). There is less of a

392 distinct topographic “uplift zone” in this model. The right edge above the underplated body,  
393 however, appears more like the reference model with its high angle normal fault (Figure 7j). The  
394 underplated body also slumps trenchward much like the reference and landsliding models.  
395 Surprisingly, the uplift data for our subduction interface model (Figure 7j) looks almost identical  
396 to the reference model but with more irregular paths, suggesting that faulting in the upper plate  
397 does not control uplift patterns as might have been expected.

398 **4. Discussion**

399 Overall our models show a clear and consistent structural and uplift framework across all  
400 underplating simulations. Faulting bounds either side of the uplifting zone directly above the  
401 underplating body. Within this uplifting zone, the highest uplift rates generally sit directly above  
402 the underplating body. The only prominent departure from this is in the erosion model, where the  
403 highest uplift rates shift trenchward in response to erosion and a reduction of overburden in the  
404 eroding region. Outboard of this uplifting zone, material moves horizontally towards the trench,  
405 whereas inboard of this zone, material is generally unaffected by the underplating process. In  
406 general, non-erosion models do not depart drastically from the reference model.

407 **4.1 Effects of Underplating**

408 The unperturbed reference model effectively demonstrates that an underplating-only  
409 regime results in antiformal uplift while also causing trenchward displacement of material  
410 outboard of the bounding normal fault. This matches modern geodetic data on the peninsula well  
411 (Thornley, 1996). In the absence of other perturbations, the mid-crustal material directly above  
412 the underplated body rises almost symmetrically, and the internal crustal boundary defines a near  
413 perfect antiform. This result is similar to what is predicted by Finite Element Models (Upton et  
414 al., 2003). The full thickness of the trenchward wedge translates horizontally towards the trench  
415 along a normal fault, with minimal uplift. The boundary (fault) dividing the antiformal uplift and  
416 trenchward displacement regimes dips trenchward and runs roughly through a point at  $x=115$   
417 km,  $y=28$  km. Once particles within the uplifting zone in the shallow (5km) and shallowest  
418 (2km) tracked layers reach this point they too begin to displace trenchward nearly horizontally.  
419 On the inboard side of uplift, a high angle thrust fault accommodates uplift in the back half of the  
420 model while insulating all material in its footwall from undergoing deformation. Thus, the entire  
421 model can be divided into three major regimes (Figure 8), a horizontal material path, a vertical

422 material path, and an unperturbed section each bounded by faults. Material can move between  
423 the different regimes and the associated uplift path will change accordingly.

424 **4.2 Effects of Changing Parameters**

425 **4.2.1 Landsliding**

426 Introducing a landslide detachment as a listric fault causes some modest changes in the  
427 deformation of the wedge. In particular, the high angle fault bounding the left side of the  
428 underplating material is guided onto the detachment, entraining more inboard particles. These  
429 particles exhibit similar horizontal paths as noted above. Otherwise, the particle paths in each of  
430 the respective zones do not change considerably. The overall pattern of faulting in the landslide  
431 model is very similar to the reference model, but results in increased trenchward displacement of  
432 material within the landslide. The main effect of surficial landsliding on the model system,  
433 therefore, is to expand the region within which material experiences horizontal displacement, and  
434 decrease the region where material undergoes vertical uplift.

435 It is interesting to note that despite being unbonded and frictionless, the imposed  
436 landslide does not have a large amount of offset. Most of the offset is localized at the steep  
437 upslope end of the listric fault. We interpret this to reflect a limitation of our model materials,  
438 which exhibit relatively high residual strength due to the interlocking of the spherical particles.  
439 In contrast, the Whakoau Fault on Raukumara Peninsula is thought to be composed of  
440 overpressured smectitic clays (Thornley, 1996). The platy nature of these clays and the presence  
441 of overpressure may make the fault weaker than we are able to replicate here. In that case, we  
442 would expect more displacement along the listric interface than we observe here. More  
443 displacement would lead to a greater reduction of overburden on the trenchward side of the  
444 uplifting zone, and could lead to more asymmetrical uplift similar to what is observed in the  
445 erosion model. Therefore, we have reservations about the ability of our modeling approach here  
446 to accurately reflect the effects of the actively extending Whakoau Fault on Raukumara  
447 Peninsula.

448 **4.2.2 Erosion**

449 Imposing differential erosion on the trenchward side of the uplifting zone has a two-fold  
450 effect: First, it expands the region that experiences vertical uplift by incorporating more slope

451 material inboard of the now trenchward-shifted bounding normal fault. Second, the material  
452 newly incorporated into the vertical uplift zone rises more rapidly due to the decreased  
453 overburden in this area. This results in a trenchward shift of the area of maximum uplift. In all  
454 other models the zone of maximum uplift exists more or less directly above the underplated  
455 body, whereas in the erosion model this zone lies farther trenchward beneath the eroding zone.  
456 The outboard shift in the location of the model's major bounding normal fault encourages more  
457 material to remain within the expanded vertical uplift zone. Therefore erosion, more so than any  
458 other perturbation, promotes a wider zone of enhanced vertical material uplift compared to any  
459 other model.

460       This shift in maximum uplift rate appears to be driven by the change in overburden,  
461 resulting from the preferential erosion of material on one side of the uplift. On the Raukumara  
462 Peninsula, it is proposed that the Miocene and younger sediments on the east side of the uplift  
463 are eroding more rapidly compared to the Torlesse Greywacke composing the axis of the  
464 Raukumara Range. Wilson (2006) nicely demonstrates the correlation between lithologies and  
465 elevation across the peninsula, adding credence to the idea that differential erodibility might be  
466 driving asymmetrical uplift. This is, interestingly, despite the fact that the more erodible  
467 lithologies lie on the leeward (eastern) side of the uplift and should sit in a rain shadow  
468 compared to the windward (western) side of the Raukumara Range, which should experience  
469 orographic precipitation (Salinger, 1980). Our modeling would suggest that if these leeward  
470 sediments are preferentially being eroded due to their less resistive nature, then uplift should  
471 localize in this direction and away from a point directly above the underplating. Although  
472 erodibility and sediment fluxes have not been quantified and compared between lithologies, a  
473 simple thermochronometric transect perpendicular to the axis of the Raukumara Range should be  
474 capable of estimating whether uplift and exhumation is more rapid in the zone of highest  
475 topography or on its trenchward side. This would allow us to judge the role differential erosion is  
476 currently playing on the peninsula.

477 **4.2.3 Faults – Both Imposed and Emergent**

478       The presence of discrete faults prior to underplating, either by the transport of basal  
479 material representing a subduction channel or the imposition of far-field reverse and high angle  
480 normal faults similar to those mapped, has little to no effect on uplift patterns. This surprising

481 outcome brings into question the role of pre-existing structures in uplift and deformation  
482 patterns. It also suggests our results here may be applicable to Raukumara Peninsula despite  
483 lacking thorough structural field mapping of the inland portion of the peninsula. That being said,  
484 our imposed faulting had minimal impact on the evolution of our wedge because the imposed  
485 faults were relatively far from the uplifting zone. The locations of these faults were based on the  
486 locations of currently mapped faults on the peninsula (Mezingarb and Spaden, 2003), but if  
487 large, unmapped, interior peninsula faults do exist they are not being accounted for here.

488 **4.3 Comparison of Model Results to Raukumara Peninsula**

489 As our models were designed and calibrated to approximate the Raukumara Peninsula  
490 structure and geometry, this modeling effort allows us to test the competing theories of Wilson  
491 (2006) and Litchfield et al. (2007) concerning the shape of uplift on the peninsula. Our results  
492 suggest that both proposed models of uplift are possible in an underplating regime given  
493 different perturbations acting on the system. In an unperturbed system, where underplating is the  
494 dominant driver of crustal uplift, our model results suggest that antiformal uplift centered around  
495 the underplated body is to be expected. This agrees with the Raukumara Peninsula field data  
496 compiled by Litchfield et al. (2007) and the modeling results of Upton et al. (2003). This result  
497 also appears to hold true regardless of the occurrence of pre-existing crustal faulting, which does  
498 not appear to affect uplift pathways in any obvious way. Thus, our understanding of the uplift  
499 behavior may not be dependent on poorly mapped structures within the Raukumara Range, and  
500 suggests that these results may apply in other simple underplating-driven domains.

501 In contrast, a strong differential erosion gradient across the surface of our model results  
502 in a trenchward shift in uplift as posited by Wilson (2006), based on her analyses of Pleistocene  
503 marine terraces. The reduction in overburden appears to direct the uplift paths of material,  
504 allowing for more rapid uplift underneath the eroded area. This phenomenon does not occur  
505 throughout the eroded region, however, as material further away from the underplated body still  
506 moves dominantly laterally. Only material within close proximity to the underplated body and  
507 directly beneath the rapidly eroding zone experiences the differential uplift effects. Therefore, if  
508 the Neogene sediments mapped on Raukumara Peninsula are truly eroding faster than the  
509 Torlesse Greywacke, as proposed by Wilson (2006), then a trenchward shift in uplift should be  
510 expected just east of the underplating body, but should not extend further trenchward than that,

511 regardless of the erosional regime. This modeling work outlines the necessary conditions to  
512 create antiformal vs asymmetrical uplift patterns, however, future work focused on quantifying  
513 erosional rates and sediment fluxes within the greywacke and Miocene sediments over tectonic  
514 time scales will be necessary to answer this question.

515         Surficial landsliding, although in essence another form of surficial material transfer  
516 similar to erosion, does not appear to have the same impact in our models. Rather than increase  
517 rates of material uplift, modeled landsliding simply incorporates more material into the lateral  
518 displacement path seen by the most trenchward monitored slope material. That being said, the  
519 displacement accommodated on our landslide detachment is minimal compared to the mapped  
520 Whakoau Fault, which Thornley (1996) proposed accommodated multiple kilometers of shallow  
521 trenchward extension. Our landslide, as it is developed in this model, is more of a minor surficial  
522 feature despite being unbonded and frictionless. We suggest that surficial landsliding and  
523 shallow crustal extension, if present, occur in response to underplating uplift, rather than drive or  
524 modulate such uplift, but note that greater displacement along our landslide detachment may  
525 move enough overburden to create uplift patterns similar to the erosion model.

526 **4.4 Comparison of Model Results to Other Proposed Zones of Underplating**

527         Underplating has been proposed to occur at many other subduction zones around the world,  
528 beyond Raukumara Peninsula. These include southern Alaska (Moore et al., 1991; Fuis et al.,  
529 2008), the Cascades (Calvert et al., 2011), Costa Rica (St. Claire et al., 2016), Chile (Adams and  
530 Reuther, 2000; Krawczyk et al., 2006), Raukumara Basin (Sutherland et al., 2003), and the  
531 southern Hikurangi margin (Henrys et al., 2013). All of these settings are thought to share the  
532 same proposed tectonic underplating process: downcutting of the décollement leads to the  
533 subcretion of subduction channel sediments from the top of the downgoing plate to the bottom of  
534 the overriding plate. However, there is a large amount of variability among the systems. For  
535 example, the interpreted depth to underplating ranges from 10 to 40 km, and only at certain  
536 locales does it appear to correspond to the depth of the Moho, as suggested beneath the  
537 Raukumara Range (Eberhardt-Phillips and Chadwick, 2002). The inferred sizes of the  
538 underplated bodies also vary widely. Consistent across nearly all locales, however, is the  
539 interpretation that underplating leads to significant topography development (Fuis et al., 2008;  
540 Calvert et al., 2011; St Claire et al., 2016; Adams and Reuther, 2000; Sutherland et al., 2003;

541 Henrys et al., 2013), as well as trenchward extension as interpreted for the Raukumara example  
542 (Fuis et al., 2008; Calvert et al., 2011; St Claire et al., 2016; Adams and Reuther, 2000;  
543 Sutherland et al., 2003). Furthermore, most underplating locales are at erosive margins where the  
544 underplated sediment is often being sourced, at least partially, from erosion at the toe of the  
545 prism.

546 At the Hikurangi margin there appears to be evidence for underplating both further north and  
547 south of Raukumara Peninsula. Along the southern Hikurangi margin, Henrys et al. (2013)  
548 reports evidence for the underplating of imbricated packages of subducted sediment from a  
549 tomographic transect there. The underplated material underlies the actively growing Axial ranges  
550 of southern New Zealand. They observe an increase in the dip of the plate interface at the same  
551 location that they see evidence for underplating. The kink point is where they interpret the  
552 downcutting of the décollement and subcretion of sediments. This kink point also aligns well  
553 with the location of the intersection of the Moho and the subducting slab, agreeing well with the  
554 idea that underplating is due to a density contrast between subducted sediments and the mantle  
555 (Henrys et al., 2013).

556 Interestingly, the southern Hikurangi margin is thought to be a net accretionary margin and  
557 strongly tectonically coupled, while Raukumara Peninsula is net erosive and uncoupled (Heise et  
558 al., 2013; Litchfield et al., 2007). If both regions truly are experiencing underplating, it calls into  
559 question the relationship between the presence of a sediment channel and a poorly coupled plate  
560 interface (Eberhart-Phillips and Chadwick, 1999). It has been proposed that the weak material in  
561 a sediment channel, if present, helps to uncouple the tectonic plates, but that does not appear to  
562 be the case here as it is in Raukumara Peninsula. Henrys et al. (2013) also sees the location of  
563 underplating as the transition from a locked to slow slipping plate interface, effectively  
564 demonstrating the opposite relationship as that proposed by Eberhart-Phillips and Chadwick  
565 (1999) for Raukumara Peninsula. It also raises the question: What is the source of this sediment  
566 if not from erosion at the toe? The transect presented by Henrys et al. (2013) does not extend all  
567 the way out to the margin toe, however, so it is impossible to know how far east the imaged  
568 sediment channel extends. If it does not extend to the trench, the subduction channel material  
569 might be sourced from the base of the overlying plate during subduction. This could explain the  
570 presence of a sediment channel at the accretionary Southern Hikurangi margin as well.

571 Unfortunately, uplift rates are not available for the landward side of the axial ranges above this  
572 potential zone of underplating beyond the last glacial maximum (LGM) (Litchfield et al., 2006).  
573 Thus, we are unable to know if the shape of uplift here is antiformal or asymmetrical on longer  
574 time scales, although since the LGM, river downcutting rates suggest antiformal uplift.  
575 (Litchfield et al., 2006).

576 The northern offshore extension of the Raukumara Range is the submarine East Cape Ridge,  
577 a proposed underplating-driven uplift and associated trenchward landslide system in Raukumara  
578 Basin (Sutherland et al., 2009). The system defines a direct submarine analog to the Raukumara  
579 Range (Sutherland et al., 2009). In this area, the overriding crust shrinks to one half the thickness  
580 (~15 km) of the Raukumara Peninsula crust (~30 km) and corresponds to a trenchward shift in  
581 the intersection between the Moho and the downgoing plate, coincident with the location of the  
582 East Cape Ridge. This ridge is thought to have formed by uplift above the location of crustal  
583 underplating and accompanied by trenchward extension when the uplift becomes oversteepened.  
584 (Sutherland et al., 2009). It is thought that this process creates a cyclical crustal dynamic where  
585 uplift drives landsliding, which supplies sediments to the trench that feeds underplating that  
586 drives uplift (Scherwatch et al., 2010; Sutherland et al., 2009). It is unclear if this same model  
587 applies to Raukumara Peninsula, as the distance from uplift to trench is greater here than it is in  
588 Raukumara Basin and it is unlikely that much of the material landsliding onshore will reach the  
589 trench. Other than that, the two systems look markedly similar. The shape of uplift of East Cape  
590 Ridge is not well constrained, but assuming minimal erosion in the subaqueous environment, our  
591 modeling work would predict antiformal uplift above the zone of active underplating.

592 In southern Alaska, seismic reflection and refraction data and magnetotelluric imaging  
593 suggest that a 10 km thick body of imbricated material sits directly below the inner forearc  
594 (Moore et al., 1991; Fuis et al., 2008). It is hypothesized that these underplated bodies are  
595 composed of marine sediments emplaced around late Oligocene times and in response to lateral  
596 expansion of the accretionary prism. Coulomb wedge theory predicts that, holding wedge  
597 strength constant, lateral expansion of the wedge via accretion requires internal thickening to  
598 maintain critical taper (Davis et al., 1983; Platt, 1986). This thickening does not appear to be due  
599 to internal shortening, and so underplating is proposed to have taken on this role.

600 Interestingly, researchers see evidence for an erosive control on underplating-driven uplift  
601 patterns, specifically over the last 5 million years (Arkle et al., 2013). Thermochronometric data  
602 suggest a rapid jump in uplift rate on the windward side of the Chugach Mountains of southern  
603 Alaska since the Pleistocene. Some have interpreted this as a response to increased glaciation  
604 and glacial erosion driven by enhanced precipitation on the windward side of uplift (Arkle et al.,  
605 2013). This could prove similar to the asymmetric uplift in the Raukumara Mountains proposed  
606 by Wilson (2006), where erosion modulates underplating-driven uplift. In Alaska, orthographic  
607 precipitation and glaciation provide the nonuniform erosion patterns, while in Raukumara  
608 Peninsula, the variable erodibility of lithologies is thought to be responsible.

609 Within the Cascadia margin, a seismic tomographic study by Calvert et al. (2011) across the  
610 Olympic Peninsula reveals a ~15 km thick low velocity zone at depths of 25-40 km, just above  
611 the inferred plate interface. This low velocity zone is proposed to be subducted sediments  
612 underplated to the bottom of the North American plate. These depths line up well with Moho  
613 depths in the area, suggesting underplating here also may be Moho regulated. As has been  
614 previously mentioned, Brandon et al., (1998) uses thermochronometers to make a compelling  
615 case for erosional controls on underplating-driven exhumation rates within the accretionary  
616 prism of the Olympic Mountains here in the Cascades. Over the last 14 my, low temperature  
617 thermochronometers show most rapid exhumation in the central massif of the Olympic  
618 mountains above the underplated body and where erosion is occurring most rapidly. The  
619 thermochronometers show a bulls-eye pattern extending outward from the center of these  
620 mountains, with systematically slower exhumation rates as you move outward. Comparing this to  
621 Raukumara Peninsula, this would be the equivalent of the Torlesse Greywacke being the most  
622 rapidly eroding lithology. This is not thought to be the case but does show the ability of surface  
623 erosion patterns to control underplating-driven exhumation. Given this example in the Olympic  
624 Peninsula, it seems reasonable to assume that rapid erosion could displace the region of  
625 maximum uplift away from the axis of the mountain range relative to the underplated body, as is  
626 proposed on Raukumara Peninsula.

627 In summary, there appears to be geophysical evidence for underplating at many subduction  
628 margins around the world. It appears that these margins share a semi-consistent tectonic theme.  
629 Commonly, these underplating margins are erosive, which favors transport of subducted

630 sediments to depth where they can become subcreted to the overriding plate. In some locations,  
631 this underplating appears to be regulated by interactions with the Moho. Topographic uplift is  
632 often accompanied by trenchward extension of the uplifting region. Surface erosion, where  
633 robust thermochronometric work has been done, appears to exhibit a control on exhumation  
634 patterns, driving rapid exhumation into the most rapidly eroding areas. This holds true whether  
635 the rapid erosion sits directly above the underplated body in the highest topography (Olympic  
636 Peninsula) or is offset to one side of the uplift (Southern Alaska).

637 **4.5 Remaining Questions**

638 Following our work here, some questions still remain. For example, it is not well constrained  
639 if differential erosion is high enough across Raukumara Peninsula to force the asymmetrical  
640 uplift our erosion model predicts. A thermochronometric study using a peninsula-perpendicular  
641 transect would greatly aid in addressing that question. In addition, our modeling technique limits  
642 us in our imposition of landsliding, so it is unclear if the shallow landsliding interpreted in the  
643 area could cause greater unloading than we modeled, causing similar uplift effects as differential  
644 erosion. The observed stable zone inboard of the area of maximum uplift might also be an  
645 boundary effect due to the presence of the fixed backwall on the right side of the models. One  
646 major drawback of our simplified models is the lack of a subduction channel that brings material  
647 to depth. This precludes an investigation of how the subduction process itself might influence  
648 underplating. As an example, we cannot assess the potential for material to peel off of the  
649 subduction channel at shallower depths, where its subcretion might produce more asymmetric  
650 uplift patterns. Another oversimplification in our model comes from the flat geometry we use for  
651 the base. This basal geometry may favor normal faulting and trenchward displacement, whereas  
652 a curved base might encourage thrust faulting on both sides of uplift similar to what is seen in  
653 Alaska (Arkle et al., 2013). Future modeling work could focus on developing a complete  
654 subduction-underplating-uplift cycle on a curved base to better recreate the entire subducted  
655 sediment path and expose the overriding plate to the effects of subduction in addition to  
656 subcretion.

657 **5. Conclusions**

658 We present a first of its kind DEM underplating model and explore the effects of subcretion  
659 on upper plate deformation and the spatial variations in material uplift. We then explore the

660 effects of other factors on the system, such as surficial landsliding, differential erosion, and both  
661 imposed and emergent upper plate asperities, to study what effects, if any, these outside forcings  
662 have on the underplating system. From our suite of experiments we conclude:

- 663 1) Underplating alone drives antiformal uplift with a maximum uplift rate directly above  
664 the underplated body.
- 665 2) Differential surficial erosion has a dramatic effect on exhumation and uplift patterns  
666 and can drive a shift in the location of highest uplift rates to the area of highest  
667 erosion.
- 668 3) The presence of pre-existing faults does not appear to play a controlling role in the  
669 structural evolution or uplift patterns of the upper plate.
- 670 4) This work suggests that, in the absence of an erodibility gradient along Raukumara  
671 Peninsula, uplift would likely approximate the antiformal pattern proposed by  
672 Litchfield et al. (2006), however, if strong differential erosion forcings are active on  
673 the peninsula, then the Wilson (2006) model of uplift is likely to be occurring.

## 674 Acknowledgements

675 Farrell and Vora were supported in part through Rice University Department of Earth,  
676 Environmental, and Planetary Sciences fellowships. Computing facilities were made available  
677 through the Rice Research Computing Support Group and the Rice Center for Computational  
678 Geophysics. The authors benefitted from discussions and input from David Blank, Gary Gray,  
679 Nur Schuba, Xiaoyu Wang, Melodie French, and Colin Zelt, among others. Modeling results and  
680 information can be obtained by contacting J. Morgan at morganj@rice.edu.

## 681 References

- 682 Adam, J. and Reuther, C.D. (2000). Crustal dynamics and active fault mechanics during  
683 subduction erosion. Application of frictional wedge analysis on to the North Chilean  
684 Forearc. *Tectonophysics*, 321; 297-325.
- 685 Arkle, J. C., Armstrong, P. A., Haeussler, P. J., Prior, M. G., Hartman, S., Sendziak, K. L.,  
686 Brush, J. A. (2013). Focused exhumation in the syntaxis of the western Chugach  
687 Mountains and Prince William Sound, Alaska. *Bulletin*, 125(5-6); 776-793.
- 688 Avouac, J. P., and Burov, E. B. (1996). Erosion as a driving mechanism of intracontinental  
689 mountain growth. *Journal of Geophysical Research: Solid Earth*, 101(B8); 17747-17769.
- 690 Ballance, P. F. (1976). Evolution of the upper Cenozoic magmatic arc and plate boundary in  
691 northern New Zealand. *Earth and planetary science letters*, 28(3); 356-370.

- 692 Barnes, P. M., Lamarche, G., Bialas, J., Henrys, S., Pecher, I., Netzeband, G. L., Crutchley, G.  
693 (2010). Tectonic and geological framework for gas hydrates and cold seeps on the  
694 Hikurangi subduction margin, New Zealand. *Marine Geology*, 272(1-4); 26-48.
- 695 Barton, N., and Bandis, S. (1982). Effects of block size on the shear behavior of jointed  
696 rock. *The 23rd US symposium on rock mechanics (USRMS)*. American Rock Mechanics  
697 Association.
- 698 Bassett, D., Sutherland, R., Henrys, S., Stern, T., Scherwath, M., Benson, A., Toulmin, S.,  
699 Henderson, M. (2010). Three-dimensional velocity structure of the northern Hikurangi  
700 margin, Raukumara, New Zealand: Implications for the growth of continental crust by the  
701 subduction erosion and tectonic underplating. *G3*, 11 (10). 1-24.
- 702 Beaumont C., Fullsack P., Hamilton J. (1992) Erosional control of active compressional orogens.  
703 In: McClay K.R. (eds) *Thrust Tectonics*. Springer, Dordrecht.
- 704 Brandon, M. T., Roden-Tice, M. K., Garver, J. I. (1998). Late Cenozoic exhumation of the  
705 Cascadia accretionary wedge in the Olympic Mountains, northwest Washington  
706 State. *Geological Society of America Bulletin*, 110(8); 985-1009.
- 707 Burbank, D.W., Leland, J., Fielding, E., Anderson, R.S., Brozovic, N., Reid, M.R., Duncan, C.  
708 (1996). Bedrock incision, rock uplift, and threshold hillslopes in the northwestern  
709 Himalayas. *Nature*, 379; 505-510.
- 710 Calvert, A.J., Preston, L.A., Farahbod, A.M. (2011). Sedimentary underplating at the Cascadia  
711 mantle-wedge corner revealed by seismic imaging. *Nature Geoscience*, 4; 545-548
- 712 Clair, J. S., Holbrook, W. S., Van Avendonk, H. J., Lizarralde, D. (2016). Along-strike structure  
713 of the Costa Rican convergent margin from seismic a refraction/reflection survey:  
714 Evidence for underplating beneath the inner forearc. *G3*, 17(2); 501-520.
- 715 Clift, P.D. and Hartley, A.J. (2007). Slow rates of subduction erosion and coastal underplating  
716 along the Andean margin of Chile and Peru. *Geology*, 35 (6); 503-506.
- 717 Cundall, P. A., and Strack, O. D. (1979). A discrete numerical model for granular  
718 assemblies. *Geotechnique*, 29(1); 47-65.
- 719 Davis, D., Suppe, J., Dahlen, F. A. (1983). Mechanics of fold-and-thrust belts and accretionary  
720 wedges. *Journal of Geophysical Research: Solid Earth*, 88(B2); 1153-1172.
- 721 Dean, S. L., Morgan, J. K., Fournier, T. (2013). Geometries of frontal fold and thrust belts:  
722 Insights from discrete element simulations. *Journal of Structural Geology*, 53; 43-53.
- 723 Eberhart-Phillips, D., and Chadwick, M. (2002). Three-dimensional attenuation model of the  
724 shallow Hikurangi subduction zone in the Raukumara Peninsula, New Zealand. *Journal  
725 of Geophysical Research: Solid Earth*, 107(B2); 1-15.
- 726 Farrell, William C. (2018). Controls on Uplift in Raukumara Peninsula, New Zealand: Insights  
727 from DEM Modeling. Rice University. Masters Thesis.

- 728 Fisher, D. M., Gardner, T. W., Marshall, J. S., Sak, P. B., Protti, M. (1998). Effect of subducting  
729 sea-floor roughness on fore-arc kinematics, Pacific coast, Costa Rica. *Geology*, 26(5);  
730 467-470.
- 731 Fuis, G.S., Moore, T.E., Plafker, G., Brocher, T.M., Fisher, M.A., Mooney, W.D., Nokleberg,  
732 W.J., Page, R.A., Beaudoin, B.C., Christensen, N.I., Levander, A.R., Lutter, W.J., Saltus,  
733 R.W., Ruppert, N.A. (2008). Trans-Alaska crustal transect and continental evolution  
734 involving subduction underplating and synchronous foreland thrusting. *Geology*, 36 (3);  
735 267-270.
- 736 Guo, Y., and Morgan, J. K. (2007). Fault gouge evolution and its dependence on normal stress  
737 and rock strength—Results of discrete element simulations: Gouge zone  
738 properties. *Journal of Geophysical Research: Solid Earth*, 112(B10); 1-17.
- 739 Heise, W., Caldwell, T. G., Bertrand, E. A., Hill, G. J., Bennie, S. L., Ogawa, Y. (2013).  
740 Changes in electrical resistivity track changes in tectonic plate coupling. *Geophysical*  
741 *Research Letters*, 40(19); 5029-5033.
- 742 Heise, W., Caldwell, T.G., Hill, G.J., Bennie, S.L., Wallin, R., Bertrand, E.A. (2012).  
743 Magnetotelluric imaging of fluid processes at the subduction interface of the Hikurangi  
744 margin, New Zealand. *GRL*, 39; 1-5.
- 745 Henrys, S., Wech, A., Sutherland, R., Savage, M., Stern, T., Sato, H., Mochizuki, K., Iwasaki,  
746 T., Okaya, D., Tozer, B., Townend, J., Kurashimo, E., Iidaka, T., Ishiyama, T. (2013).  
747 SAHKE geophysical transect reveals crustal and subduction zone structure at the  
748 southern Hikurangi margin, New Zealand. *G3*, 14 (7); 2063-2083.
- 749 Kamp, P. J. (1999). Tracking crustal processes by FT thermochronology in a forearc high  
750 (Hikurangi margin, New Zealand) involving Cretaceous subduction termination and mid-  
751 Cenozoic subduction initiation. *Tectonophysics*, 307(3-4); 313-343.
- 752 Katz, O., Morgan, J. K., Aharonov, E., Dugan, B. (2014). Controls on the size and geometry of  
753 landslides: insights from discrete element numerical simulations. *Geomorphology*, 220;  
754 104-113.
- 755 Kimura, H., Takeda, T., Obara, K., Kasahara, K. (2010). Seismic evidence for active  
756 underplating below the megathrust earthquake zone in Japan. *Science*, 329; 210-212.
- 757 Kobor, J. S., and Roering, J. J. (2004). Systematic variation of bedrock channel gradients in the  
758 central Oregon Coast Range: implications for rock uplift and shallow  
759 landsliding. *Geomorphology*, 62 (3-4); 239-256.
- 760 Koons, P.O. (1990). Two-sided orogen: Collision and erosion from the sandbox to the Southern  
761 Alps, New Zealand. *Geology*, 18 (8); 679–682.
- 762 Koons, P.O., Upton, P., Barker, A.D. (2012) The influence of mechanical properties on the link  
763 between tectonic and topographic evolution. *Geomorphology*, 137; 168-180.

- 764 Krawczyk C.M. (2006). Geophysical Signatures and Active Tectonics at the South-Central  
765 Chilean Margin. In: Oncken O. et al. (eds) *The Andes. Frontiers in Earth Sciences*.  
766 Springer, Berlin, Heidelberg.
- 767 Litchfield, N., and Berryman, K., (2006). Relations between postglacial fluvial incision rates and  
768 uplift rates in the North Island, New Zealand. *JGR*, 111; 1-15.
- 769 Litchfield, N., Ellis, S., Berryman, K., Nicol, A. (2007). Insights into subduction-related uplift  
770 along the Hikurangi Margin, New Zealand, using numerical modeling. *Journal of*  
771 *Geophysical Research: Earth Surface*, 112(F2); 1-17.
- 772 Mazengarb C, Speden IG (compilers) 2000. Geology of the Raukumara area: scale 1:250,000 .  
773 Lower Hutt: Institute of Geological and Nuclear Sciences 1:250,000 geological map 6.  
774 60 p+1 folded map.
- 775 McNamara, D. D., Sewell, S., Buscarlet, E., Wallis, I. C. (2016). A review of the Rotokawa  
776 geothermal field, New Zealand. *Geothermics*, 59; 281-293.
- 777 Mielke, P., Weinert, S., Bignall, G., Sass, I. (2016). Thermo-physical rock properties of  
778 greywacke basement rock and intrusive lavas from the Taupo Volcanic Zone, New  
779 Zealand. *Journal of Volcanology and Geothermal Research*, 324; 179-189.
- 780 Moore, J.C., Diebold, J., Fisher, M.A., Sample, J., Brocher, T., Talwani, M., Ewing, J., von  
781 Heune, R., Rowe, C., Stone, D., Stevens, C., Sawyer, D. (1991). EDGE deep seismic  
782 reflection transect of the eastern Aleutian arc-trench layered lower crust reveals  
783 underplating and continental growth. *Geology*, 19; 420-424.
- 784 Morgan, J. K. (2015). Effects of cohesion on the structural and mechanical evolution of fold and  
785 thrust belts and contractional wedges: Discrete element simulations. *Journal of*  
786 *Geophysical Research: Solid Earth*, 120(5); 3870-3896.
- 787 Morgan, J. K., and McGovern, P. J. (2005). Discrete element simulations of gravitational  
788 volcanic deformation: 1. Deformation structures and geometries. *Journal of Geophysical*  
789 *Research: Solid Earth*, 110(B5); 1-22.
- 790 Naylor, M., Sinclair, H. D., Willett, S., Cowie, P. A. (2005). A discrete element model for  
791 orogenesis and accretionary wedge growth. *Journal of Geophysical Research: Solid*  
792 *Earth*, 110(B12); 1-16.
- 793 Nicol, A., and Beavan, J. (2003). Shortening of an overriding plate and its implications for slip  
794 on a subduction thrust, central Hikurangi Margin, New Zealand. *Tectonics*, 22(6); 1-14.
- 795 Nicol, A., Mazengarb, C., Chanier, F., Rait, G., Uruski, C., Wallace, L. (2007). Tectonic  
796 evolution of the active Hikurangi subduction margin, New Zealand, since the  
797 Oligocene. *Tectonics*, 26(4); 1-24.
- 798 Pedley, K.L. (2010). Modelling submarine landscape evolution in response to subduction  
799 processes, Northern Hikurangi Margin, New Zealand. University of Canterbury. Doctoral  
800 Thesis.

- 801 Platt, J. P. (1986). Dynamics of orogenic wedges and the uplift of high-pressure metamorphic  
802 rocks. *Geological society of America bulletin*, 97(9); 1037-1053.
- 803 Rait, G., Chanier, F., Waters, D. W. (1991). Landward-and seaward-directed thrusting  
804 accompanying the onset of subduction beneath New Zealand. *Geology*, 19(3); 230-233.
- 805 Reyners, M., Eberhart-Phillips, D., Stuart, G. (1999). A three-dimensional image of shallow  
806 subduction: Crustal structure of the Raukumara Peninsula, New Zealand. *Geophysical  
807 Journal International*, 137(3); 873-890.
- 808 Sak, P. B., Fisher, D. M., Gardner, T. W., Marshall, J. S., LaFemina, P. C. (2009). Rough crust  
809 subduction, forearc kinematics, and Quaternary uplift rates, Costa Rican segment of the  
810 Middle American Trench. *Geological Society of America Bulletin*, 121(7-8); 992-1012.
- 811 Salinger, M. J. (1980). New Zealand climate: I. precipitation patterns. *Monthly weather  
812 review*, 108(11); 1892-1904.
- 813 Scherwath, M., Kopp, H., Flueh, E. R., Henrys, S. A., Sutherland, R., Stagpoole, V. M.,  
814 Dannowski, A. (2010). Fore-arc deformation and underplating at the northern Hikurangi  
815 margin, New Zealand. *Journal of Geophysical Research: Solid Earth*, 115(B6); 1-23.
- 816 Stewart, S. W. (2007). Rock mass strength and deformability of unweathered closely jointed  
817 New Zealand greywacke. University of Canterbury. Masters Thesis.
- 818 Sutherland, R., Stagpoole, V., Uruski, C., Kennedy, C., Bassett, D., Henrys, S., Barker, D.  
819 (2009). Reactivation of tectonics, crustal underplating, and uplift after 60 Myr of passive  
820 subsidence, Raukumara Basin, Hikurangi-Kermadec fore arc, New Zealand: Implications  
821 for global growth and recycling of continents. *Tectonics*, 28(5); 1-23.
- 822 Thiede, R. C., Bookhagen, B., Arrowsmith, J. R., Sobel, E. R., Strecker, M. R. (2004). Climatic  
823 control on rapid exhumation along the Southern Himalayan Front. *Earth and Planetary  
824 Science Letters*, 222(3-4), 791-806.
- 825 Thornley, S. (1996) Neogene tectonics of Raukumara Peninsula, Northern Hikurangi Margin,  
826 New Zealand. Victoria University of Wellington. Doctoral Thesis.
- 827 Upton, P., Koons, P. O., Eberhart-Phillips, D. (2003). Extension and partitioning in an oblique  
828 subduction zone, New Zealand: Constraints from three-dimensional numerical  
829 modeling. *Tectonics*, 22(6); 1-14.
- 830 Walcott, R.I. (1987). Geodetic strain and the deformational history of the North Island of New  
831 Zealand during the late Cainozoic. *Phil. Trans of Royal Society of Longon. A.* 321; 163-  
832 181.
- 833 Wessel, P., and Smith, W. H. (1995). New version of the generic mapping tools. *Eos,*  
834 *Transactions American Geophysical Union*, 76(33); 329-329.
- 835 Whipple, K. X. (2009) "The influence of climate on the tectonic evolution of mountain  
836 belts." *Nature geoscience*, 2.2 (97); 97-104.

837 Wilson, K.J. (2006) Mechanisms of late Quaternary coastal uplift along the Raukumara  
838 Peninsula segment of the Hikurangi margin, North Island, New Zealand. Victoria  
839 University of Wellington. Doctoral Thesis.

840

841

842

843

844

845

846

847

848

849

850

851

852

853

854

855

856

857

858

859

860

861

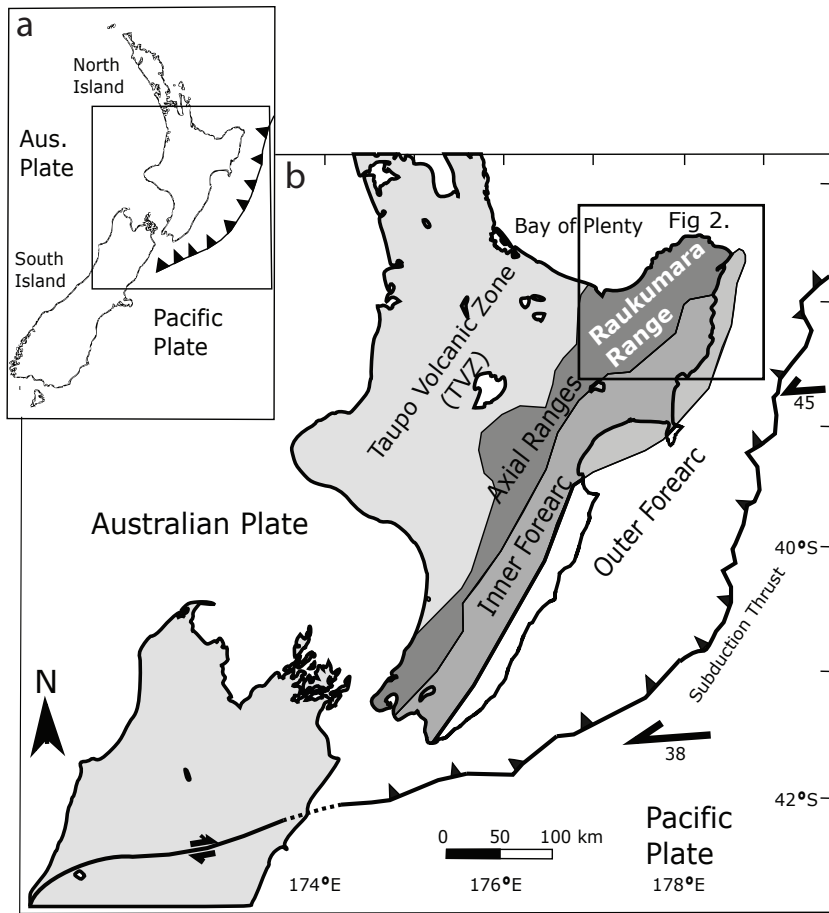
862

863

864

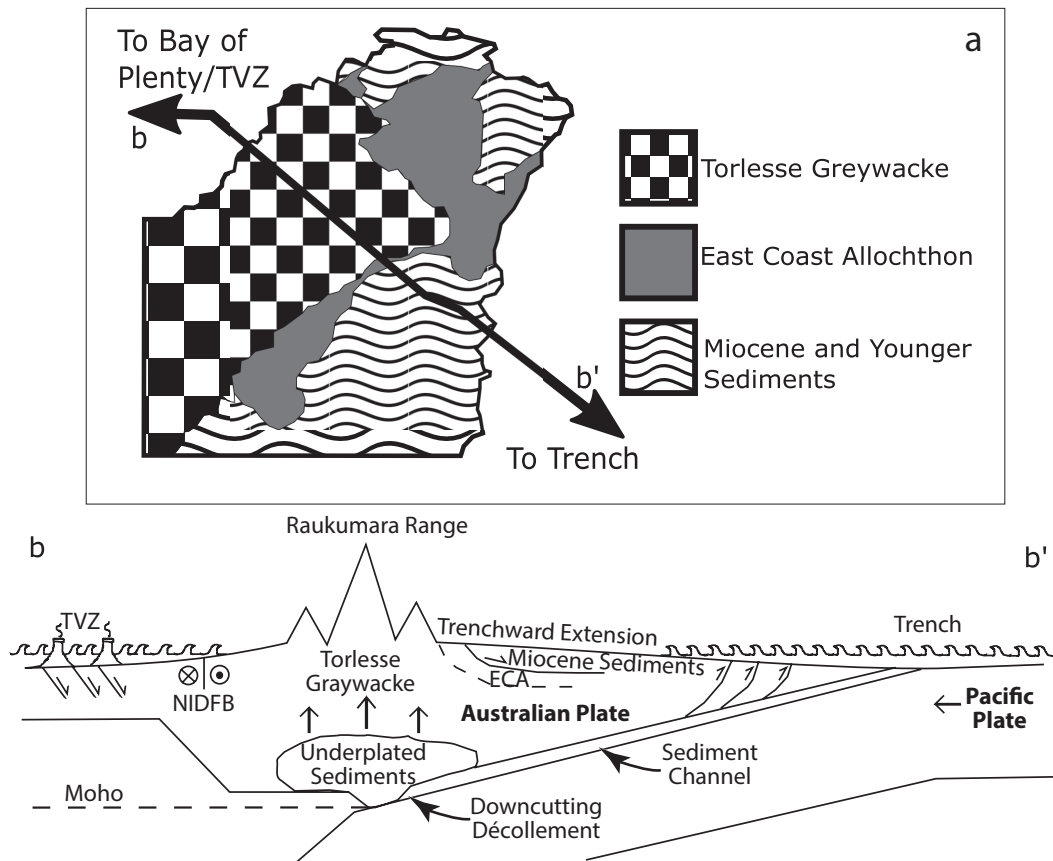
865

**Figure (with caption below and on the same page)**



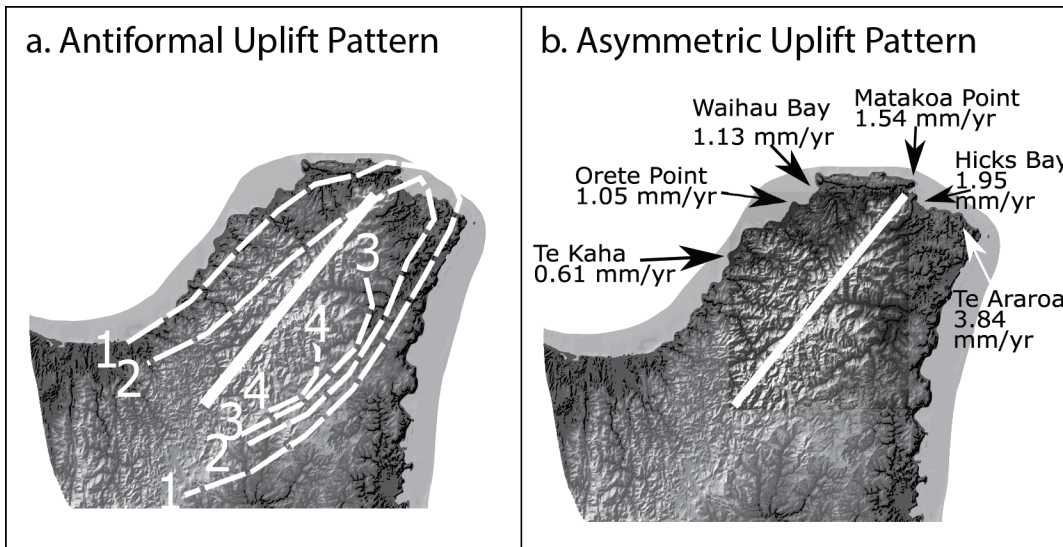
**Figure 1:** (a) Geography and tectonic setting of New Zealand. Box shows area of map in part (b). (b) Tectonic setting of the North Island. Modified from Litchfield et al. (2007).

**Figure (with caption below and on the same page)**



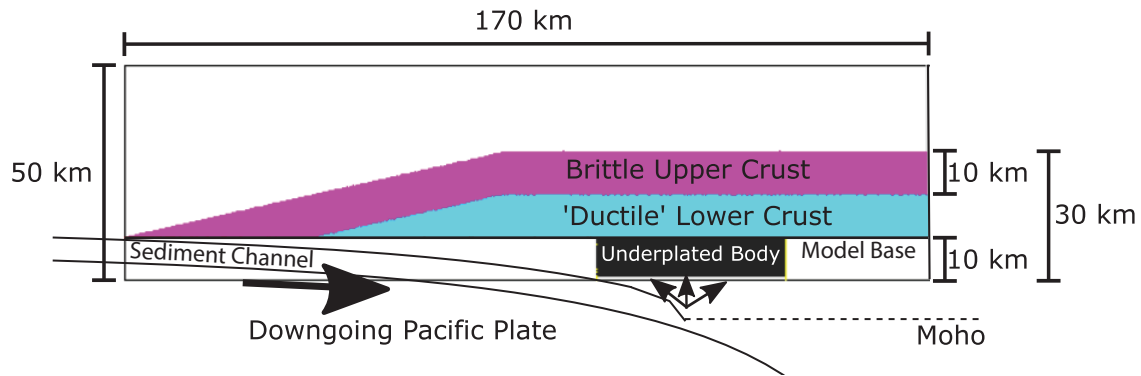
**Figure 2:** (a) Simplified lithologies of Raukumara Peninsula. Note the location of the d-d' schematic transect. Modified from Wilson, 2006. (b) Schematic cross section from the Hikurangi trench, across Raukumara Peninsula, to the Taupo Volcanic Zone (TVZ). NIDFB – North Island Dextral Fold Belt. ECA – East Coast Allochthon

**Figure (with caption below and on the same page)**



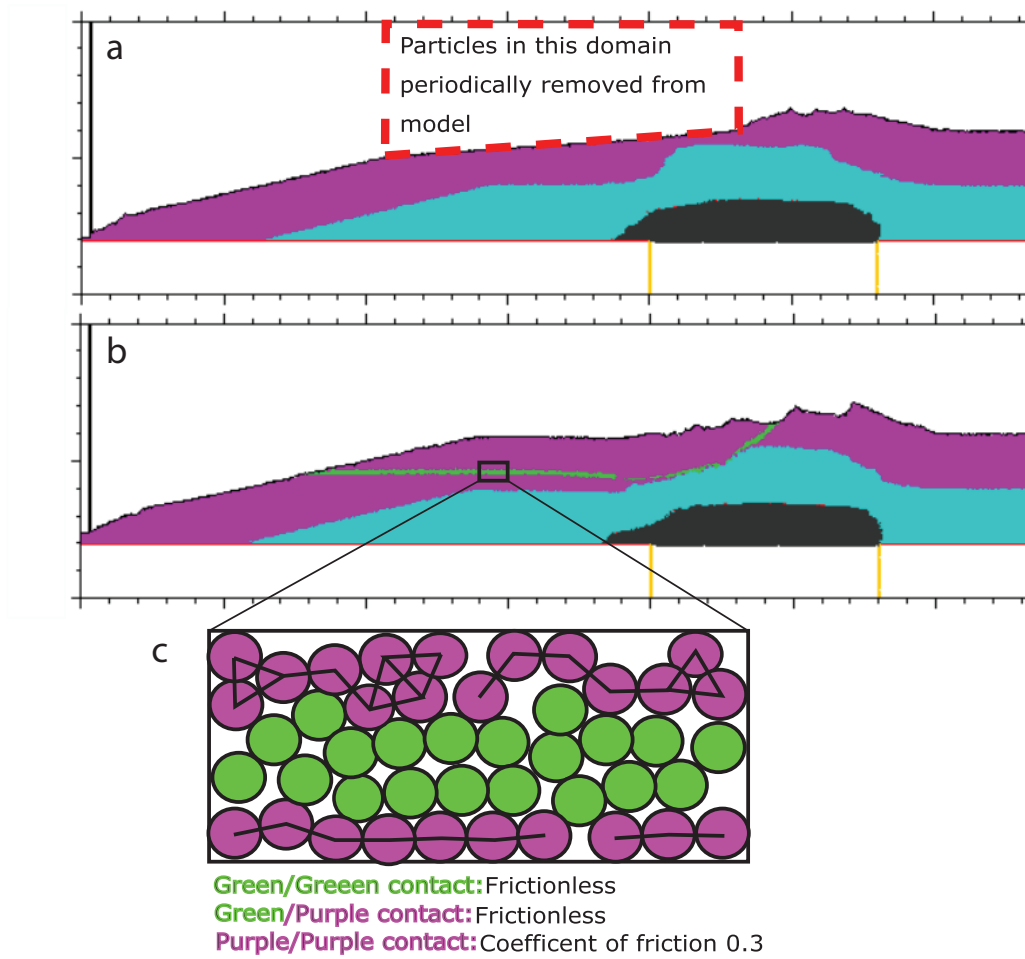
**Figure 3:** Alternative models on the Pleistocene-Modern uplift patterns of the Raukumara Range. (a) Uplift rates (in mm/yr) since the Pleistocene, documented by Litchfield et al., (2007). These rates were determined from Pleistocene fluvial terraces and show roughly antiformal uplift around the topographic high and axis of Raukumara Range (solid white bar). (b) Locations of Pleistocene marine terraces studied by Wilson (2006), giving their calculated uplift rate for the last 125 ky. These data suggest that the most rapidly uplifting part of the peninsula is 13 km east (trenchward) of the Raukumara Range, at Te Araroa.

**Figure (with caption below and on the same page)**



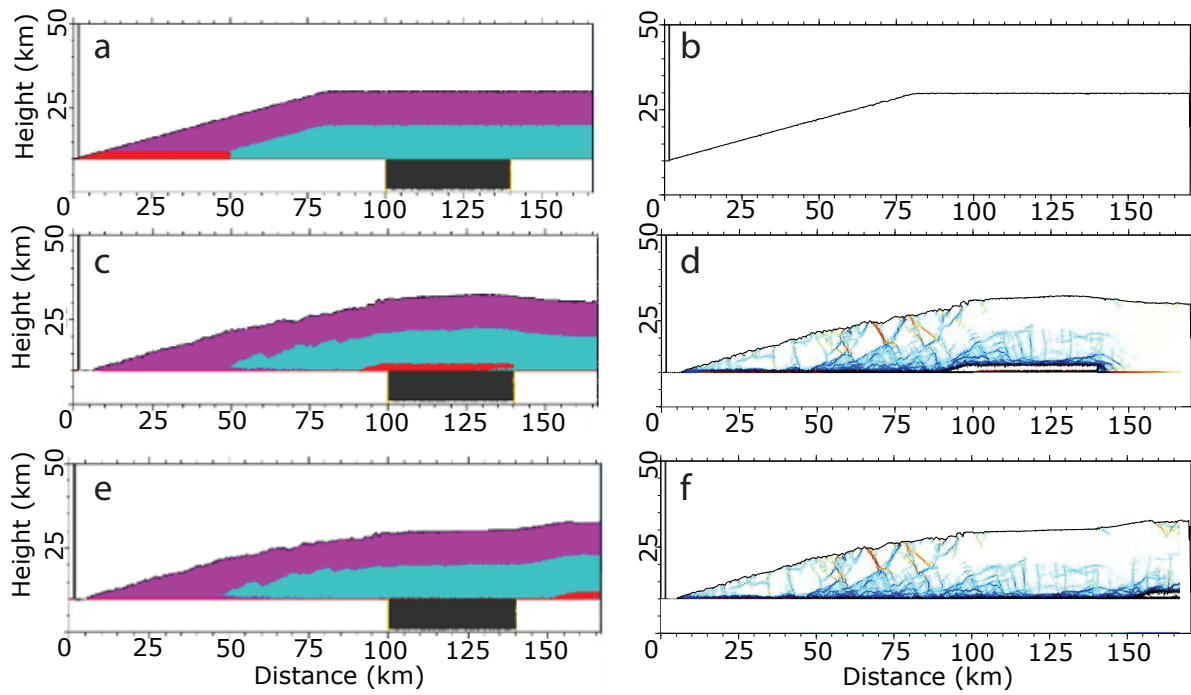
**Figure 4:** Configuration of reference model for all simulations presented here. The underplated body is pushed up into the two-layered crust above as a proxy for underplating of material derived from a sediment channel on the downgoing plate. Underplating is thought to occur when the sediments reach Moho depths. See Table 1 for geomechanical parameters of the underplated body, lower, and upper crust and see text for description of modeling technique.

Figure (with caption below and on the same page)



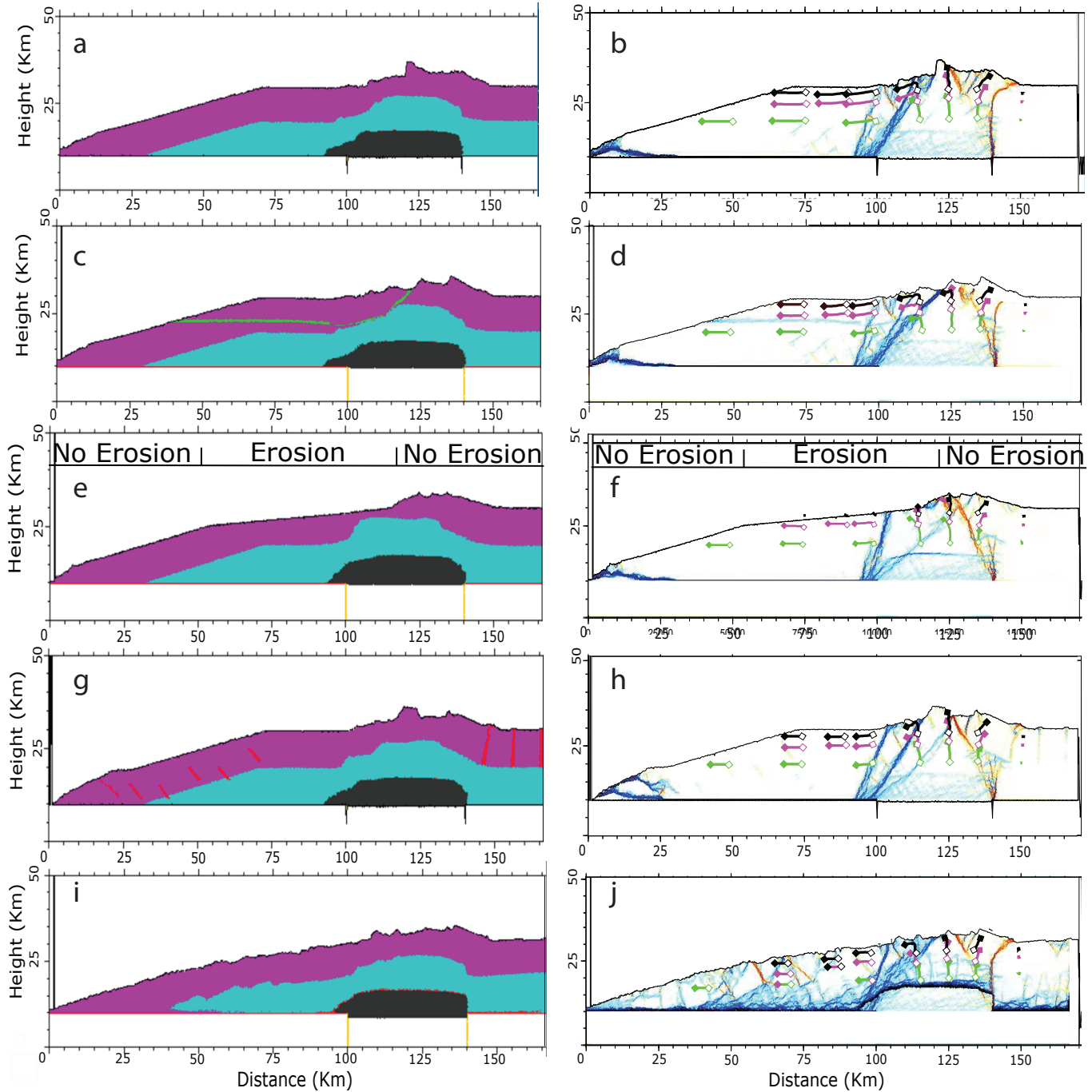
**Figure 5:** (a) Schematic diagram showing how erosion is imposed on the model. Particles that enter the red dashed box via surficial uplift are periodically removed from the system. (b) Schematic diagram showing how weak zones are introduced (e.g., landslide detachment as shown here). Particle domains (e.g., layers, rectangles, etc., shown in green here) are selected, and their properties are changed. In this example, interparticle bonds (black lines) are removed, and interparticle friction is reduced to zero for interactions between selected particles (green), and with the surrounding wedge (purple). This encourages deformation along this weak interface.

**Figure (with caption below and on the same page)**



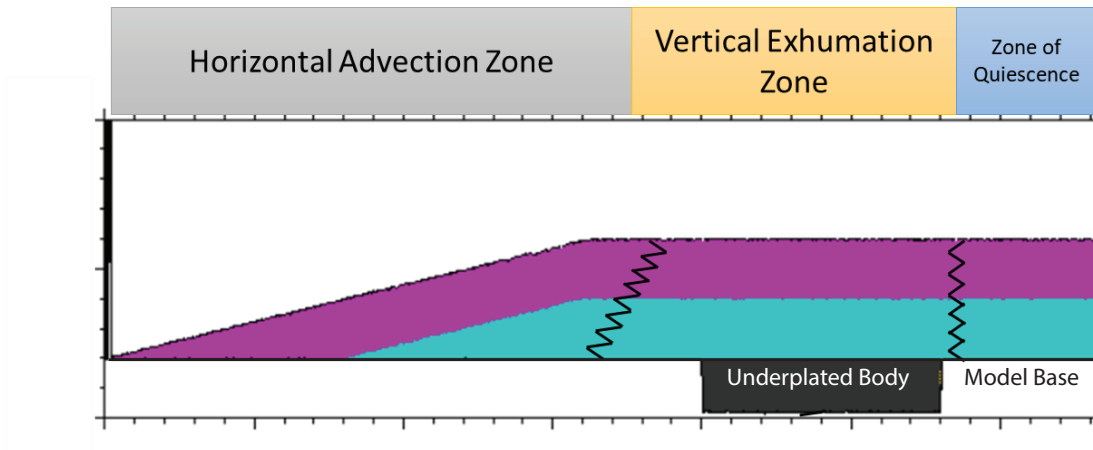
**Figure 6:** Sequential images of deformation resulting from basal advection and corresponding distortional strain. In the particle position images (a, c, e) red material slides along base of model, preconditioning the wedge prior to underplating. The strain plots (b, d, f) show cumulative distortional strain at each of these time points. Red colors indicate top to the right shear, blue colors indicate top to the left shear, with stronger color intensities indicating greater displacement.

Figure (with caption below and on the same page)



**Figure 7:** a) Final particle configuration of reference model, for underplating only. (b) Distortional strain field and particle uplift paths for reference model. For all distortional strain plots: Color intensity denotes zones of high shear strain; blue indicates top to the left sense of shear, and red indicates top to the right sense of shear. Green, purple, and black lines are the travel paths of individual particles starting at 10, 5, and 2 km depth, respectively. Open diamonds show initial positions while closed diamonds show final positions. (c) Final particle position of landslide model. (d) Distortional strain field and particle uplift paths for landslide model. (e) Final particle configuration for erosion model. (f) Distortional strain field and particle uplift paths for erosion model. Note that many particles originating at 2km depth are eroded before any displacement can occur. (g) Final particle configuration of imposed faulting model. (h) Distortional strain field and particle uplift path for imposed faulting model. (i) Final particle configuration of basal advection model. (j) Distortional strain field and particle uplift path for basal advection model. This includes distortional strain from both the basal advection and underplating portions of the model. See Figure 6 for more on how wedge was preconditioned for the basal advection model.

**Figure (with caption below and on the same page)**



**Figure 8:** Generalized model of underplating-driven deformation, showing three distinct uplift zones and two main faults that occur in all models. The different perturbations we applied alter the boundaries between these three uplift zones or the style of faulting between them, but do not change the general patterns.